

# Multiscale transitional flow in anisotropic nanoparticle suspensions revealed by time-resolved x-ray scatter microscopy

Kesavan Sekar<sup>1</sup>, Viney Ghai<sup>1</sup>, Reza Ghanbari<sup>1,2,a</sup>, Marko Bek<sup>1,3</sup>, Marianne Liebi<sup>4,5,6</sup>,  
Aleksandar Matic<sup>4,7</sup>, Ann E. Terry<sup>2,3</sup>, Kim Nygård<sup>2,3\*</sup>, Roland Kádár<sup>1,2,3,7\*</sup>

<sup>1</sup>Department of Industrial and Materials Science, Chalmers University of Technology, SE-412 96, Gothenburg, Sweden.

<sup>2</sup>MAX IV Laboratory, Lund University, SE-224 84, Lund, Sweden.

<sup>3</sup>LINXS Institute of Advanced Neutron and X-ray Science, SE-224 84, Lund, Sweden.

<sup>4</sup>Department of Physics, Chalmers University of Technology, SE-412 96, Gothenburg, Sweden.

<sup>5</sup>Division of Photon Science, Paul Scherrer Institute, CH-5232, Villigen, Switzerland.

<sup>6</sup>Institute of Materials, Ecole Polytechnique Fédérale de Lausanne (EPFL), CH-1015, Lausanne, Switzerland.

<sup>7</sup>Wallenberg Wood Science Center (WWSC), Chalmers University of Technology, SE-412 96, Gothenburg, Sweden.

<sup>a</sup>Present address: NKT Technology Consulting, Västerås, Sweden.

\*Corresponding author(s). E-mail(s): [kim.nygard@maxiv.lu.se](mailto:kim.nygard@maxiv.lu.se); [roland.kadar@chalmers.se](mailto:roland.kadar@chalmers.se);

## Abstract

Complex fluids transition from laminar to transitory flow above a critical control parameter, akin to their Newtonian counterparts. In a continuum mechanics sense, fluid elements follow the ensuing complex trajectories, giving rise to secondary flows in terms of macroscopic vortices and patterns thereof. However, if we replace idealized fluid elements with actual anisotropic nanoparticles, would their trajectories still reveal the same spatiotemporal behavior as the macroscopic flow field? This question is fundamental for complex fluids, where fully developed turbulence is suppressed by high viscosities and where understanding particle–flow coupling is central to transport, processing, and structure formation. To address this question, we develop small-angle x-ray scatter microscopy of unprecedented temporal resolution combined with polarized light imaging, thereby bridging seven orders of magnitude in lengthscales. Proof-of-principle is demonstrated on a classical stability problem, Taylor-Couette flow, of platelet-like graphene oxide nanoparticle and rod-like cellulose nanocrystal suspensions. The analysis shows hitherto hidden, markedly different multiscale dynamics underlying flow stability; while the platelet-like particles follow the wavy motion of the macroscopic, secondary flow field, the rod-like particles exhibit high-frequency motion that is uncorrelated with the vortex instabilities.

**Keywords:** Laminar-turbulent transition, Taylor-Couette instabilities, Multiscale spectral dynamics, Time-resolved small-angle x-ray scatter microscopy

The transition from laminar to turbulent flow in complex fluids is a longstanding multiscale problem within classical physics, characterized by strong coupling between lengthscales several orders of magnitude apart [1, 2]. One of the benchmark laboratory-scale experiments for characterizing such transitions is Taylor-Couette flow

between concentric cylinders [3], with the inner cylinder rotating and the outer cylinder at rest. It can be argued that pioneering studies date back to Maxwell’s first unsuccessful attempts at flow-induced birefringence in a concentric cylinder setup, without any surviving details of his experimental setup whereby ‘a solid cylinder could be made to rotate’ inside a ‘cylindrical box with a glass bottom’ [4], decades before the seminal experiments of Couette, Mallock, and Taylor [5]. With increasing Reynolds number  $Re$ , describing the ratio between inertial to viscous forces, the fluid transitions from laminar to featureless turbulent flow via a cascade of increasingly complex, macroscopic vortex instabilities [6–10]. In laminar Couette flow (LCF) a fluid element (in continuum mechanics sense) follows a simple circular trajectory. In the presence of flow disturbances at a critical  $Re$ , the trajectories will re-organize at first into three-dimensional helicoidal trajectories forming counter-rotating toroidal vortices, known as Taylor vortex flow (TVF), separated by radial outflow and inflow regions [10]. Further increasing  $Re$  results in wavy vortex flow (WVF), modulations thereof (modulated wavy vortices, MWV), chaotic merging and splitting of vortices (chaotic wavy vortices, CWV), before the onset of turbulent flow regimes in the form of turbulent wavy vortices (TWV) and turbulent Taylor vortices (TTV). We note that this simple pattern-development scenario is characteristic for both Newtonian fluids and the complex ones studied here, although (de)stabilization of non-Newtonian fluids can induce new instability modes [11].

Considering the particular case of anisotropic nanoparticles in the aforementioned complex transitional flow fields, several aspects must be considered. Generally, a mechanistic understanding of their non-equilibrium flow behavior requires multiscale structural characterization [12, 13]. Beyond the onset of instabilities, the presence of spatiotemporally varying, macroscopic flow fields are expected to cause intricate, position-dependent alignment of dispersed anisotropic particles [14]. Depending on nanoparticle morphology and flow field, different nanoparticle symmetry axes may align with the flow as described below. However, while the macroscopic flow field can be resolved with various flow visualization or particle image velocimetry methods, these observations take place significantly above lengthscales that can be associated with the smallest vortical structures in transitional flows [15].

Spatially resolved small-angle x-ray scattering (hereafter denoted SAXS microscopy) has developed into an important experimental technique for mapping of nanoscale constituents [16–19], widely applicable to different aggregation states of the sample and complex in-situ experiments. Indeed, Philippe et al. [20] reported pioneering SAXS microscopy experiments on suspensions of platelet-like clay nanoparticles in Taylor-Couette flow, thereby identifying time-averaged alignment of the nanoparticles’ director and their effect on the onset of instabilities. However, the modest temporal resolution in state-of-the-art SAXS microscopy of about a minute has so far limited the technique to spatiotemporal mapping of relatively slow processes, such as assembly of nanoparticle superlattices [21] or in-operando electrode sodiation [22].

Here we develop SAXS microscopy of unprecedented, millisecond temporal resolution, making use of the extreme x-ray flux offered by diffraction-limited synchrotron sources [23] and analysis in the frequency domain. Inspired by recent advances in multiscale analysis of complex fluids under shear flow [24–26], we further quantify the macroscopic Taylor-Couette flow patterns and their dynamics by polarized light imaging (PLI), utilizing

intrinsic flow-induced birefringence of the nanoparticle suspensions [11]. We can thereby address an outstanding multiscale challenge in transitional Taylor-Couette flow: if we conceptually replace a fluid element (in the continuum sense) with an anisotropic nanoparticle, will we find the same spatiotemporal motion at macroscopic and nanoscopic scales? By combining PLI and SAXS microscopy observations of two nanostructured fluids with platelet- and rod-like nanoparticle morphologies in Taylor-Couette flow, we show for the first time instability modes where transitional flow effects at nanoparticle level co-exist with molecular motion effects, apparently depending on the particle morphology and/or aspect ratio.

## Custom Taylor-Couette-PLI-SAXS setup

The current experiment is based on a custom Taylor-Couette flow cell presented in Figs. 1a and 1b, where throughout this study we make use of rotating inner and stationary outer cylinders. In this geometry, PLI and SAXS experiments are carried out in different configurations [12, 27]. On the one hand, PLI is employed in the radial configuration, visualizing the macroscopic flow in the plane defined by the velocity ( $\mathbf{v}$  or 1) and vorticity ( $z$ ,  $\nabla \times \mathbf{v}$ , or 3) directions. On the other hand, SAXS data are collected in the tangential configuration, probing the scattering plane defined by the velocity gradient ( $\nabla \mathbf{v}$  or 2) and vorticity directions, while averaging the data over the velocity direction. We note that the choice of SAXS configuration is usually based on nanoparticle morphology; platelet-like particles predominantly align normal to the velocity gradient and are thus optimally studied in tangential configuration [20, 28], whereas rod-like particles align in the velocity direction and are hence preferably studied in radial scattering configuration [29, 30]. Nevertheless, in the presence of secondary flows as studied here, the tangential scattering configuration is suitable for both particle morphologies (see Supplementary Fig. S6 for a quantitative comparison of scattering configurations). We emphasize that combined PLI and SAXS microscopy in Taylor-Couette geometry on a common millisecond timescale, as developed here and depicted in Fig. 1c, is critical to address transitional flow across lengthscales.

We study two morphologically distinct nanoparticle suspensions - platelet-like graphene oxide (GO) and rod-like cellulose nanocrystals (CNC). Their static nanoscale structure can be inferred from time-averaged SAXS data collected under laminar Couette flow (LCF) as presented in Supplementary Fig. S7; whereas the GO data decrease monotonously with scattering vector modulus  $q$ , without any signature of liquid-crystalline (or even short-range) ordering observed for GO at higher concentrations either under flow [28] or in equilibrium [31], indicating that we are probing individual nanoparticles, the CNC data exhibit distinct maxima in the structure factor at  $q_{\max} \approx 0.16 \text{ nm}^{-1}$ , corresponding to local ordering at  $2\pi/q_{\max} \approx 40 \text{ nm}$  interparticle distance. Throughout this study we average the SAXS data for both suspensions in the scattering vector range  $q_0 = 0.13 - 0.20 \text{ nm}^{-1}$ .

The prominent peak in the structure factor of the CNC SAXS data raises the question of probed lengthscale. For example, equilibrium suspensions exhibit slowing down of diffusivity at intermediate  $q$ , while retaining single-particle dynamics at larger  $q$  [32, 33], an effect sometimes colloquially coined de Gennes narrowing following Ref. [34] (despite the different underlying physics between diffusion of suspended nanoparticles and dynamics of

atomic/molecular systems [35]). In the present case, however, the qualitatively different nanoparticle dynamics observed for platelet-like GO versus rod-like CNC (discussed below) are not due to local ordering, as evidenced by the  $q$ - and concentration-dependent CNC data of Supplementary Fig. S6.

## Multiscale analysis of supercritical flow patterns

To make macroscale PLI flow pattern and SAXS nanoscale observations directly comparable, we have developed a common spatiotemporal analysis framework as illustrated in Fig. 2. For PLI, single pixel lines along the  $z$  axis of the cylinders are combined from the frames of video recordings (panel a) to form macroscopic space-time diagrams (panel b), exemplified for the CNC suspension subjected to MWV. This particular instability mode exhibits (i) spatial periodicity along the vorticity direction as well as (ii) high-frequency periodicity and (iii) low-frequency modulation in the time domain. Spatial and temporal two-dimensional Fourier analysis thereof following Refs. [11, 36] yield the characteristic spatial wavenumber  $\kappa$  and temporal frequencies  $f_n$  versus Reynolds number  $Re$ . For SAXS microscopy, in turn, two-dimensional scattering patterns acquired at the same frame rate with PLI are azimuthally integrated over  $q$  (panel c) to construct azimuthal angle ( $\Phi$ ) - time diagrams corresponding to each of the  $z = ct$ . scans (panel d). Expanding the standard approach for characterizing nanoparticle flows by small-angle scattering, see e.g. Refs. [26, 27, 37], we base our analysis on a *spatially* and *temporally* resolved variant of the Hermans orientation parameter [38],

$$P_2(z, t) = \frac{\int_0^\pi \frac{1}{2} (3 \cos^2 \Phi - 1) I(\Phi, z, t)_{q_0} \sin \Phi d\Phi}{\int_0^\pi I(\Phi, z, t)_{q_0} \sin \Phi d\Phi}. \quad (1)$$

Here,  $I(\Phi, z, t)_{q_0}$  denotes the spatially and temporally resolved annular scattering pattern along the azimuthal angle  $\Phi$  (defined clockwise with respect to the velocity gradient direction, see Fig. 2c), averaged over the above specified scattering vector range  $q_0$ . We note that  $P_2(z, t)$  provides an instantaneous, ensemble-averaged, and local measure of the preferred alignment and degree thereof of the suspended nanoparticles. The current choice of azimuthal integration limits is particularly useful for studying Taylor-Couette instabilities; positive and negative values of  $P_2(z, t)$  indicate that the projection of the nanoparticles' director in the scattering plane preferentially aligns in the vorticity and velocity gradient directions, respectively. Alternatively we could determine the preferential alignment of the nanoparticles' director,  $\varphi(z, t)$ , as outlined in the Methods section and shown in Supplementary Fig. S6. In either case, subsequent Fourier analysis allows quantitative comparison with macroscopic PLI data. The SAXS scans in the  $z$  direction are scaled to the wavenumbers determined from PLI analysis, to cover one and a half adjacent vortices ( $\Delta z$  is a pair of vortices).

## Onset of instabilities

As alluded to in the introduction, transitional flow proceeds via a sequence of increasingly complex macroscopic vortex instabilities with increasing Reynolds number  $Re$ . For rheologically complex fluids as studied here (see Supplementary Fig. S8 for shear viscosities of the investigated suspensions), the detailed onset and order of the

instability transitions depend on an intricate interplay between shear-thinning and elasticity effects, a detailed discussion of which is beyond the scope of the present paper. Nevertheless, we summarize a few aspects of their flow stability. Laminar Couette flow (LCF) transitions at a critical Reynolds number  $Re_{cr1}$  to Taylor vortex flow (TVF), a time-invariant axisymmetric instability mode consisting of counter-rotating toroidal vortices defined by one characteristic wavenumber  $\kappa$  along  $z$  but no temporal frequency  $f_n$ . Fig. 3 exemplifies the LCF-TVF transition as visualized by PLI and SAXS. The presence of GO has a destabilizing effect on the onset of instabilities, with  $Re_{cr1}^{GO} < Re_{cr1}^{Newt} \approx 144$ . Furthermore, the transition to TVF is initially an elasticity-modified pattern as mentioned above. Supercritical modes are Newtonian-like, although significant differences are observed for other boundary conditions [39]. CNC, in turn, has a stabilizing effect on the flow, with  $Re_{cr1}^{CNC} > Re_{cr1}^{Newt}$ , while shear-thinning effects lead to smaller characteristic TVF wavenumbers than for the reference Newtonian case. All supercritical flow patterns are Newtonian-like, albeit with onset and range of  $Re$  differing considerably compared to the Newtonian case [11].

Before proceeding further, we briefly discuss the onset of the present instabilities and validate our observations with expected results based on the available scientific literature. For GO and CNC subjected to LCF, the space-time diagrams in the left panel of Figs. 3a and 3c (radial configuration) confirm the absence of any discernible macroscopic flow patterns. Focusing instead on the time-averaged azimuthal SAXS data of the middle panel, GO shows pronounced peaks at  $\Phi = 0$  and  $180^\circ$ , while for CNC no significant scattering is observed in the tangential configuration. Qualitatively speaking, the nanoparticles primarily scatter x-rays parallel to their short axis, providing direct access to their alignment. This confirms the expected scenario; GO and CNC nanoparticles predominantly align with their long axes perpendicular to  $\nabla \mathbf{v}$  and parallel to  $\mathbf{v}$ , respectively. Turning next to GO subjected to Taylor vortex flow, the nanoplatelets preferentially align vertically (vorticity direction,  $\nabla \times \mathbf{v}$ ) in the radial inflow / outflow regions, akin to previous observations for suspensions of platelet-like particles in TVF [20]. The inside of the vortices can be identified by variations in the orientation direction, Fig. 3b. We further note that the TVF pattern debuts with higher wavenumbers (decreased height of the vortices) and then settles for lower wavenumbers. The CNC data of Fig. 3d, in contrast, shows distinct patterns in both PLI and SAXS visualization at the onset of TVF, with the nanoparticle director following the macroscopic vortex in its toroidal trajectory.

## Supercritical instability modes

Next we proceed to the sequence of vortex instabilities, as outlined briefly in the introduction and detailed in Table 1. Fig. 4 compares modulated wavy vortex flow at similar  $Re$  in both suspensions. In the left panel of Fig. 4a we apply the above developed multiscale characterization on the platelet-like GO suspension, noting a remarkable similarity between the macroscopic flow field and the alignment of the nanoparticle director in terms of both spatial and temporal periodicity. For comparison we also present corresponding data for the rod-like CNC suspension in Fig. 4b, displaying markedly different spatiotemporal evolution at macroscopic and nanoscopic scales; while the CNC director exhibits the same spatial periodicity as the macroscopic flow field, it

shows no signature of large-scale wavy dynamics. Further examples underscoring the discrepancy are presented in Supplementary Fig. S9.

The spatially and temporally resolved nanoscale orientation parameters above are determined from sequences of position-dependent SAXS time series. While data synchronization by cross correlation is possible (at least for GO), we have concluded that the similarity between PLI and SAXS is captured without the need for synchronization of the relatively high frequency of the wavy oscillations. Nevertheless, in order to facilitate quantitative analysis of the multiscale dynamics, we present in the middle panels of Fig. 4 the power spectral density of the spatiotemporal orientation parameter,

$$S(z, f) = \lim_{t_0 \rightarrow \infty} t_0^{-1} |\mathcal{F}[P_2(z, t) - \langle P_2(z) \rangle_t]|^2, \quad (2)$$

where  $f$  denotes the frequency and  $\mathcal{F}$  the temporal Fourier transform taken over the time window  $t_0$ . Here we subtract for convenience the temporally averaged orientation parameter,  $\langle P_2(z) \rangle_t = t_0^{-1} \int_0^{t_0} P_2(z, t) dt$ , in order to suppress the zeroth Fourier component. While such Fourier analysis is readily applicable for PLI as it requires acquisition frame rates that are accessible in many commercial optical cameras, the temporal resolution has been so far a limiting factor in SAXS analysis. For both GO and CNC we observe distinct spectral dynamics, markedly different from the broadband power spectral density  $\propto f^{-2}$  expected for (rotational) Brownian motion. Since we observe no shift in the characteristic frequencies with position along the vorticity direction, we also present in the right panels the spatially averaged power spectral densities  $\langle S(f) \rangle_z = (\kappa/0.75) \int_0^{0.75\kappa^{-1}} S(z, f) dz$ . For GO we observe a single  $f_n \approx 8$  Hz excitation and its higher harmonics, whereas for CNC we observe an  $f_n \approx 29$  Hz excitation and a weak signature of the  $f_\Omega \approx 7$  Hz rotation of the inner cylinder of the Taylor-Couette cell. In both cases, the nanoparticle excitations constitute motion centered around the mean director schematically depicted in the right panel of Figs. 3b and 3d, distinctly different from the tumbling, precessing, and rolling motion expected for such suspension in shear flow between planar surfaces [40].

To further emphasize this remarkable finding, we correlate in Fig. 5 the characteristic macroscopic and nanoscopic frequencies as probed by PLI and SAXS, respectively. The multiscale dynamics of GO and CNC are found to behave markedly different across all instability modes investigated. The GO nanoplatelets follow the wavy motion of the macroscopic flow field. For TVF we cannot identify a single characteristic temporal frequency, as expected based on PLI data, whereas the slower modulation frequency of the MWV instability seems to fall outside the spatiotemporal window of the present SAXS experiment. In contrast, the CNC director oscillates with a significantly higher frequency, apparently neither correlated with the macroscopic flow field nor a higher harmonic of the rotational frequency  $f_\Omega$ . We note that the CNC data are reminiscent of recent simulation results of rod-like particles aligning along the local tangent of the Taylor-Couette geometry [14], although the latter results were obtained for different concentration and dimensions of the suspended particles. We foresee that these experimental results will stimulate further simulation studies on this topic.

## Discussion

We can partly understand the strikingly different multiscale spatiotemporal behavior of platelet-like GO versus rod-like CNC suspensions by considering the balance between flow-induced rotational motion, in the form of the macroscopic wavy mode acting as a 'forcing' frequency on the nanoparticles, and de-orientation due to Brownian motion, as expressed by the rotational diffusion coefficient  $D_r$ . Together they constitute a rotational supercritical flow Péclet number,  $Pe_{r,sc}^{(w)} = f_{n,PLI}/D_r$ . In this interpretation,  $Pe_{r,sc}^{(w)} \gg 1$  implies that supercritical-flow-induced effects dominate and therefore the particles align with the flow, in contrast to  $Pe_{r,sc}^{(w)} \ll 1$  for which Brownian motion dominates. Interestingly, we obtain  $Pe_{r,sc}^{(w)} \propto 10^1$  for GO and  $\propto 10^{-1}$  for CNC, respectively, clearly separating the two regimes.

The detailed impact of the elucidated multiscale dynamics on the flow stability and the classical macroscopic interpretation thereof in terms of elastic and shear thinning effects remains to be determined. The fact that GO shows evidence of fluid elasticity effects at the transition to TVF while mostly shear-thinning effects are plausibly assigned to CNC is intriguing. Likewise, despite both GO and CNC suspensions showing Newtonian-like flow patterns, GO stabilizes and CNC destabilizes the onset of instabilities, akin to the platelet-like Oldroyd-A and rod-like Oldroyd-B models [41]. Understanding this multiscale interplay could have significant ramifications, e.g., for suppression or enhancement of certain modes using nanoscale material design.

Finally, vortex instabilities in Taylor-Couette flow also serve as a model for instability-induced pattern formation [42], a phenomenon of orderly self-organization ranging from snow flakes [43] to cortical convolutions [44]. These are often multiscale in nature, with some degrees of freedom at small lengths participating in pattern formation at macroscopic scales, although explicit multiscale modeling of pattern formation is scarce [45]. A key question then is which small-scale degrees of freedom are relevant for macroscopic pattern formation and which can be coarse-grained out? Given the markedly different multiscale dynamics of GO and CNC reported above, we foresee explicit studies on how nanoparticle morphology affect macroscopic pattern formation in transitional flow.

## Methods

### Materials

Graphene oxide (Highly acidic 20 % aqueous paste from Abalonyx; short axis  $d = 1 \pm 0.5$  nm; long axis  $l = 2 \pm 1$   $\mu$ m) was dispersed in Milli-Q water using an Elmasonic P30H bath sonicator at 37 KHz frequency for 30 minutes. Cellulose nanocrystals (CelluForce NCC<sup>®</sup>NCV100-NASD90;  $d = 6 \pm 2$  nm;  $l = 230 \pm 70$  nm) were dispersed in Milli-Q water using Branson Sonifier 450 (20 kHz ultrasonic horn with a 1/2" diameter probe tip) operating at an amplitude of 60 % with a duty cycle of 60 % for 30 minutes. Both suspensions were placed in an ice bath to prevent sample heating and replenished frequently.

Supplementary Fig. S8 presents the shear viscosity  $\eta$  of both suspensions. The GO data are well described by a power-law model,  $\eta(\dot{\gamma}) = K \cdot \dot{\gamma}^{n-1}$ , where  $\dot{\gamma}$  is the shear rate,  $K$  a prefactor, and  $n$  the power index. The

CNC data, in turn, can be described by the Carreau-Yasuda model [46],  $\eta(\dot{\gamma}) = \eta_\infty + (\eta_0 - \eta_\infty) [1 + (\lambda\dot{\gamma})^a]^{\frac{n-1}{a}}$ , with  $\eta_0$  and  $\eta_\infty$  denoting the viscosities at zero and infinite shear rates, respectively,  $\lambda$  the characteristic time,  $a$  the transition parameter, and  $n$  the power index.

Rotational diffusion coefficients were estimated [46] based on the classical thin-disk approximation in Stokes flow for GO,  $D_r^{GO} = 3k_B T / 8\pi\eta l^3$ , and on the slender-rod approximation for CNC,  $D_r^{CNC} = 3k_B T (\ln(l/d)) / \pi\eta l^3$ , where  $k_B = 1.38 \times 10^{-23}$  J/K and all experiments carried out at room temperature,  $T = 296$  K. The ensuing rotational diffusion coefficients,  $D_r^{GO} \approx 0.16$  and  $D_r^{CNC} \approx 94$  s<sup>-1</sup>, are in good agreement with previous experimental estimations [47, 48].

## Custom flow cell

The experiments were performed using a custom Taylor-Couette cell specifically designed for flow visualization. The cell was mounted on an Anton Paar MCR702 Multidrive rheometer in dual motor configuration and counter-movement mode, with only the inner cylinder rotating. In the combined PLI and SAXS experiment both cylinders were made of polycarbonate in order to minimize parasitic SAXS scattering, while the PLI data presented above were collected in a separate PLI experiment using a polycarbonate inner and glass outer cylinder for improved visibility. The inner and outer cylinders have radii of  $R = 20.5$  and  $R_1 = 22.5$  mm, respectively, with the gap ratio  $\epsilon = R/R_1 = 0.91$ , while the cell height is  $L = 68.7$  mm (cf. Fig. 1b for geometrical definitions of the flow cell). We determined the dimensionless Reynolds number,  $Re = \rho R \Omega \delta / \eta$ , using rheological data, with  $\delta$  denoting the gap width,  $\Omega$  the angular velocity of the inner cylinder, and  $\rho$  the density of the suspension. As an alternative quantification of inertial to viscous forces, we also present in Table 1 the dimensionless Taylor number,  $Ta = \rho^2 R \Omega^2 \delta^3 / \eta^2$ .

## Polarized light imaging (PLI)

The PLI experiment was carried out using an optical setup with two orthogonal linear polarizers placed upstream and downstream of the custom Taylor-Couette flow cell. In brief, we recorded flow visualization videos in the velocity-vorticity plane versus Reynolds number at 100 Hz for 1800 s, from which we generated space-time plots. We carried out spatial and temporal analysis by performing two-dimensional fast Fourier transforms (FFTs) of the space-time plots and averaging over the temporal and spatial frequencies, respectively. The use of intrinsic flow-induced birefringence of the nanoparticle suspensions yields similar characteristic frequencies as standard visualization particles [36]. For more details on the PLI experiments, we refer to Ref. [11].

## Small-angle x-ray scattering (SAXS)

The SAXS experiment was carried out at the ForMAX beamline of the MAX IV Laboratory [49], making use of the high-flux multilayer monochromator setup and the EIGER2 X 4M [50] photon-counting pixel detector  $\approx 1.8$  m downstream of the sample. We employed an incident x-ray beam of  $\approx 5 \times 10^{14}$  photons s<sup>-1</sup>, with an energy of 16.3 keV and a moderate beam size of  $\approx 200 \times 200$   $\mu\text{m}^2$  at the sample position. For each sample and

Taylor-Couette instability, we mapped the instabilities along the vorticity direction in 14 steps in the range of  $0 - 0.75\kappa_{PLI}^{-1}$ , i.e., covering approximately one and a half vortices, with  $\kappa_{PLI}$  being the wavenumber of each instability as determined from spatial Fourier analysis of the PLI data ( $\kappa_{PLI}^{-1} \approx 5 - 10$  mm depending on sample and instability mode). In each position, we sampled a SAXS time series at 100 Hz for 4 s, during which we observed radiation damage in neither SAXS nor torque data. Finally, we estimated the power spectral density of the spatially and temporally resolved orientation parameter  $P_2(z, t)$  using Welch’s method of overlapped segment averaging.

As an alternative to SAXS analysis based on the spatiotemporal Hermans orientation parameter  $P_2(z, t)$  of Eq. (1), we also determined the local and instantaneous angle of the nanoparticles’ director,  $\varphi(z, t) = \arctan(\Im(a_1)/\Re(a_1)) + \pi/2$ , the degree thereof,  $|a_1|/|a_0|$ , and the scattering power,  $|a_0|$ , where  $\Re$  and  $\Im$  denote real and imaginary parts of a complex quantity and  $a_i = a_i(z, t)$  the  $i$ th complex FFT component of  $I(\Phi, z, t)_{q_0}$  along the azimuthal dimension  $\Phi$  (see Supplementary Fig. S6a). Such FFT-based analysis will be highly advantageous in future applications of the present methodology to two-dimensional scans composed of  $\geq 10^5$  SAXS patterns.

The Taylor-Couette geometry warrants a brief discussion. Both PLI and SAXS probes an orientation projection of a complex, three-dimensional and time-dependent flow field, averaged over the velocity gradient and velocity directions in the radial and tangential configurations, respectively. In the tangential case, SAXS analysis is further complicated by the curvature of the geometry ( $\leq 17^\circ$ ) along the x-ray beam path, partly smearing out the signal from nanoparticle alignment. Nevertheless, the identical nanoscale dynamics observed in both scattering configurations, as exemplified in Supplementary Fig. S6b, support the interpretation that the nanoparticle director dynamics probed by SAXS in tangential configuration can be quantitatively compared to the macroscopic dynamics probed by PLI in radial configuration.

**Acknowledgements.** Research conducted at MAX IV, a Swedish national user facility, is supported by the Swedish Research Council under contract 2018-07152, the Swedish Governmental Agency for Innovation Systems under contract 2018-04969, and Formas under contract 2019-02496. The work was supported by Chalmers Foundation through the project Chalmers Center for Advanced Neutron and X-ray scattering techniques in cooperation with MAX IV. K.S., V.G., M.B., and R.K. are grateful for the financial support of the Wallenberg Wood Science Center (WWSC), FibRe Vinnova Competence Center, 2D-TECH Vinnova Competence Centre and Chalmers Areas of Advance Materials Science, Nano and Production. The authors thank Alexandra Aulova, Ases A. Mishra, and Sajjad Pashazadeh for assistance during the SAXS experiments. The authors are grateful to Prof. Gareth McKinley for helpful remarks on dimensionless scaling.

## References

- [1] Sreenivasan, K.R.: Fluid turbulence. *Rev. Mod. Phys.* **71**, 383–395 (1999)
- [2] Warhaft, Z.: Turbulence in nature and in the laboratory. *Proc. Natl. Acad. Sci. USA* **99**, 2481–2486 (2002)

- [3] Taylor, G.I.: VIII. Stability of a viscous liquid contained between two rotating cylinders. *Phil. Trans. Royal Soc. London* **A223**, 289–343 (1923)
- [4] Maxwell, J.C.: IV. On double refraction in a viscous fluid in motion. *Proc. R. Soc. Lond.* **22**, 46–47 (1874)
- [5] Donnelly, R.J.: Taylor-Couette flow: The early days. *Physics Today* **4**, 32–39 (1991)
- [6] Wendt, T.: Turbulente strömungen zwischen zwei rotierenden konaxialen zylindern. *Ing. Arch.* **4**, 577–595 (1933)
- [7] Gollub, J.P., Swinney, H.L.: Onset of turbulence in a rotating fluid. *Phys. Rev. Lett.* **35**, 927–930 (1975)
- [8] Andereck, C.D., Liu, S.S., Swinney, H.L.: Flow regimes in a circular Couette system with independently rotating cylinders. *J. Fluid Mech.* **164**, 155–183 (1986)
- [9] Baumert, B.M., Muller, S.J.: Flow regimes in model viscoelastic fluids in a circular Couette system with independently rotating cylinders. *Phys. Fluids* **9**, 566–586 (1997)
- [10] Wereley, S., Lueptow, R.: Spatio-temporal character of non-wavy and wavy Taylor-Couette flow. *J. Fluid. Mech.* **364**, 59–80 (1998)
- [11] Ghanbari, R., Pashazadeh, S., Sekar, K., Nygård, K., Terry, A., Liebi, M., Matic, A., Kádár, R.: Painting Taylor vortices with cellulose nanocrystals: suspension flow supercritical spectral dynamics. *Phys. Fluids* **36**, 044114 (2024)
- [12] Vermant, J., Solomon, M.J.: Flow-induced structure in colloidal suspensions. *J. Phys.: Condens. Matter* **17**, 187–216 (2005)
- [13] Kádár, R., Sprik, S., Nypelö, T.: Cellulose nanocrystal liquid crystal phases: progress and challenges in characterization using rheology coupled to optics, scattering, and spectroscopy. *ACS Nano* **15**, 7931–7945 (2021)
- [14] Assen, M.P.A., Ng, C.S., Will, J.B., Stevens, R.J.A.M., Lohse, D., Verzicco, R.: Strong alignment of prolate ellipsoids in Taylor–Couette flow. *J. Fluid Mech.* **935**, 7–1 (2022)
- [15] Tokgoz, S., Elsinga, G.E., Delfos, R., Westerweel, J.: Spatial resolution and dissipation rate estimation in Taylor–Couette flow for tomographic PIV. *Exp. Fluids* **53**, 561–583 (2012)
- [16] Bunk, O., Bech, M., Jensen, T.H., Feidenhans'l, R., Binderup, T., Menzel, A., Pfeiffer, F.: Multimodal x-ray scatter imaging. *New J. Phys.* **19**, 123016 (2009)
- [17] Feldkamp, J.M., Kuhlmann, M., Roth, S.V., Timmann, A., Gehrke, R., Shakhverdova, I., Paufler, P., Filatov, S.K., Bubnova, R.S., Schroer, C.G.: Recent developments in tomographic small-angle x-ray scattering.

- [18] Liebi, M., Georgiadis, M., Menzel, A., Schneider, P., Kohlbrecher, J., Bunk, O., Guizar-Sicairos, M.: Nanostructure surveys of macroscopic specimens by small-angle scattering tensor tomography. *Nature* **527**, 349–352 (2015)
- [19] Schaff, F., Bech, M., Zaslansky, P., Jud, C., Liebi, M., Guizar-Sicairos, M., Pfeiffer, F.: Six-dimensional real and reciprocal space small-angle x-ray scattering tomography. *Nature* **527**, 353–356 (2015)
- [20] Philippe, A.M., Baravian, C., Jenny, M., Meneau, F., Michot, L.J.: Taylor-Couette instability in anisotropic clay suspensions measured using small-angle x-ray scattering. *Phys. Rev. Lett.* **108**, 254501 (2012)
- [21] Yu, Y., Yu, D., Sadigh, B., Orme, C.A.: Space- and time-resolved small angle x-ray scattering to probe assembly of silver nanocrystal superlattices. *Nat. Commun.* **9**, 4211 (2018)
- [22] Olsson, M., Klein, A., Mozhukhona, N., Xiong, S., Appel, C., Carlsen, M., Nielsen, L., Rensmo, L., Liebi, M., Matic, A.: Resolving the sodiation process in hard carbon anodes with nanostructure specific x-ray imaging. *Adv. Sci.* **12**, 08635 (2025)
- [23] Eriksson, M., van der Veen, J.F., Quitmann, C.: Diffraction-limited storage rings - a window to the science of tomorrow. *J. Synchrotron Rad.* **21**, 837–842 (2014)
- [24] Dunderdale, G.J., Davidson, S.J., Ryan, A.J., Mykhaylyk, O.O.: Flow-induced crystallisation of polymers from aqueous solution. *Nat. Commun.* **11**, 3372 (2020)
- [25] Bianco, S., Stewart, F.H., Panja, S., Zyar, A., Bowley, E., Bek, M., Kádár, R., Terry, A., Appio, R., Plivelic, T.S., Maguire, M., Poptani, H., Marcello, M., Sonani, R.R., Egelman, E.H., Adams, D.J.: Forging out-of-equilibrium supramolecular gels. *Nat. Synth.* **3**, 1481 (2024)
- [26] Ghanbari, R., Terry, A., Wojno, S., Bek, M., Sekar, K., Sonker, A.K., Nygård, K., Ghai, V., Bianco, S., Liebi, M., Matic, A., Westman, G., Nypelö, T., Kádár, R.: Propagation of orientation across lengthscales in sheared self-assembling hierarchical suspensions via Rheo-PLI-SAXS. *Adv. Sci.* **12**, 2410920 (2025)
- [27] Eberle, A.P.R., Porcar, L.: Flow-SANS and Rheo-SANS applied to soft matter. *Curr. Opin. Coll. Interface Sci.* **17**, 33–43 (2012)
- [28] Poulin, P., Jalili, R., Neri, W., Nallet, F., Divoux, T., Colin, A., Aboutalebi, S.H., Wallace, G., Zakri, C.: Superflexibility of graphene oxide. *Proc. Natl. Acad. Sci. USA* **113**, 11088–11093 (2016)
- [29] Pignon, F., Challamel, M., De Geyer, A., Elchamaa, M., Semeraro, E.F., Hengl, N., Jean, B., Putaux, J.-L., Gicquel, E., Bras, J., Prevost, S., Sztucki, M., Narayanan, T., Djeridi, H.: Breakdown and buildup mechanisms of cellulose nanocrystal suspensions under shear and upon relaxation probed by SAXS and

SALS. Carbohydrate Polymers **260**, 117751 (2021)

- [30] Munier, P., Hadi, S.E., Segad, M., Bergström, L.: Rheo-SAXS study of shear-induced orientation and relaxation of cellulose nanocrystal and montmorillonite nanoplatelet dispersions. *Soft Matter* **18**, 390–396 (2022)
- [31] Xu, Z., Gao, C.: Aqueous liquid crystals of graphene oxide. *ACS Nano* **5**, 2908–2915 (2011)
- [32] Nägele, G.: On the dynamics and structure of charge-stabilized suspensions. *Phys. Rep.* **272**, 215–372 (1996)
- [33] Nygård, K., Buitenhuis, J., Kagias, M., Jefimovs, K., Zontone, F., Chushkin, Y.: Anisotropic de Gennes narrowing in confined fluids. *Phys. Rev. Lett.* **116**, 167801 (2016)
- [34] de Gennes, P.G.: Liquid dynamics and inelastic scattering of neutrons. *Physica A* **25**, 825 (1959)
- [35] Ackerson, B.J., Pusey, P.N., Tough, R.J.A.: Interpretation of the intermediate scattering function at short times. *J. Chem. Phys.* **76**, 1279–1282 (1982)
- [36] Dutcher, C.S., Muller, S.J.: The effects of drag reducing polymers on flow stability: Insights from the Taylor-Couette problem. *Korea-Aust. Rheol. J.* **21**, 213–223 (2009)
- [37] Håkansson, K.M.O., Fall, A.B., Lundell, F., Yu, S., Krywka, C., Roth, S.V., Santoro, G., Kwick, M., Wittberg, M.P., Wågberg, L., Söderberg, L.D.: Hydrodynamic alignment and assembly of nanofibrils resulting in strong cellulose filaments. *Nat. Commun.* **5**, 4018 (2014)
- [38] Hermans, P.H., Booy, J.D.: Beiträge zur kenntnis des deformationsmechanismus und der feinstruktur der hydratzellulose: X. die Kratky'sche kette als rechenmodell für den deformationsmechanismus der hydratzellulosegele. *Kolloid-Zeitschrift* **88**, 73–78 (1939)
- [39] Sekar, K., Ghai, V., Ghanbari, R., Nygård, K., Terry, A., Kádár, R.: Influence of nanoparticle morphologies in Taylor-Couette flow transitions (2025). Manuscript in preparation
- [40] Huang, H., Yang, X., Krafczyk, M., Lu, X.-Y.: Rotation of spheroidal particles in Couette flows. *J. Fluid Mech.* **692**, 369–394 (2012)
- [41] Hillebrand, F., Hill, R.J., Davoodi, M., Haward, S.J., Shen, A.Q., Poole, R.J., Varchanis, S.: Flat elastic disc suspensions are indistinguishable from solutions of long flexible polymers within planar incompressible flows. *Phys. Rev. Lett.* **135**, 024002 (2025)
- [42] Cross, M.C., Hohenberg, P.C.: Pattern formation outside of equilibrium. *Rev. Mod. Phys.* **65**, 851–1112 (1993)

- [43] Ben-Jacob, E., Garik, P.: The formation of patterns in non-equilibrium growth. *Nature* **343**, 523–530 (1990)
- [44] Tallinen, T., Chung, J.Y., Rousseau, F., Girard, N., Lefèvre, J., Mahadevan, L.: On the growth and form of cortical convolutions. *Nature Phys.* **12**, 588–593 (2016)
- [45] Würthner, L., Brauns, F., Pawlik, G., Halatek, J., Kerssemakers, J., Dekkers, C., Frey, E.: Bridging scales in a multiscale pattern-forming system. *Proc. Natl. Acad. Sci. USA* **119**, 2206888119 (2022)
- [46] Larson, R.G.: *The Structure and Rheology of Complex Fluids*. Oxford University Press, Oxford, New York (1999)
- [47] Kim, S.G., Wang, S.H., Ok, C.M., Jeong, S.Y., Lee, H.S.: Lateral diffusion of graphene oxides in water and the size effect on the orientation of dispersions and electrical conductivity. *Carbon* **125**, 280–288 (2017)
- [48] Van Rie, J., Schütz, C., Gencer, A., Lombardo, S., Gasser, U., Kumar, S., Salazar-Alvarez, G., Kang, K., Thielemans, W.: Anisotropic diffusion and phase behavior of cellulose nanocrystal suspensions. *Langmuir* **35**, 2289–2302 (2019)
- [49] Nygård, K., McDonald, S.A., González, J.B., Haghghat, V., Appel, C., Larsson, E., Ghanbari, R., Viljanen, M., Silva, J., Malki, S., Li, Y., Silva, V., Weninger, C., Engelmann, F., Jeppsson, T., Felcsuti, G., Rosén, T., Gordeyeva, K., Söderberg, L.D., Dierks, H., Zhang, Y., Yao, Z., Yang, R., Asimakopoulou, E.M., Rogalinski, J.K., Wallentin, J., Villanueva-Perez, P., Krüger, R., Dreier, T., Bech, M., Liebi, M., Bek, M., Kádár, R., Terry, A.E., Tarawneh, H., Ilinski, P., Malmqvist, J., Cerenius, Y.: ForMAX - a beamline for multiscale and multimodal structural characterization of hierarchical materials. *J. Synchrotron Rad.* **31**, 363–377 (2024)
- [50] Donath, T., Jung, D.Š., Burian, M., Radicci, V., Zambon, P., Fitch, A.N., Dejoie, C., Zhang, B., Ruat, M., Hanfland, M., Kewish, C.M., Riessen, G.A., Naumenko, D., Amenitsch, H., Bourenkov, G., Bricogne, G., Chari, A., Schulze-Briese, C.: EIGER2 hybrid-photon-counting x-ray detectors for advanced synchrotron diffraction experiments. *J. Synchrotron Rad.* **30**, 723–738 (2023)

**Table 1** Main characteristics of the studied Taylor-Couette instabilities: laminar Couette flow (LCF), Taylor vortex flow (TVF), wavy vortex flow (WVF), modulated wavy vortex flow (MWV), and turbulent wavy vortex flow (TWV). Data are presented for both GO and CNC in terms of rotational frequency  $f_\Omega$  of the Taylor-Couette cell, Reynolds number  $Re$ , Taylor number  $Ta$ , and rotational supercritical Peclet number  $Pe_{r,sc}$ .

Sample	Instability	$f_\Omega$	$Re$	$Ta$	$Pe_{r,sc}^{(w)}$
GO	LCF	0.47 Hz	60	209	–
	TVF	1.08 Hz	112	1237	–
	WVF	1.34 Hz	142	1954	20
	MWV	2.17 Hz	237	5465	41
	TWV	3.27 Hz	368	13194	64
CNC	LCF	3.25 Hz	124	1267	–
	TVF	6.18 Hz	248	6009	–
	MWV	7.05 Hz	289	8214	0.096
	MWV	8.65 Hz	370	13332	0.10
	TWV	11.49 Hz	516	25952	0.13

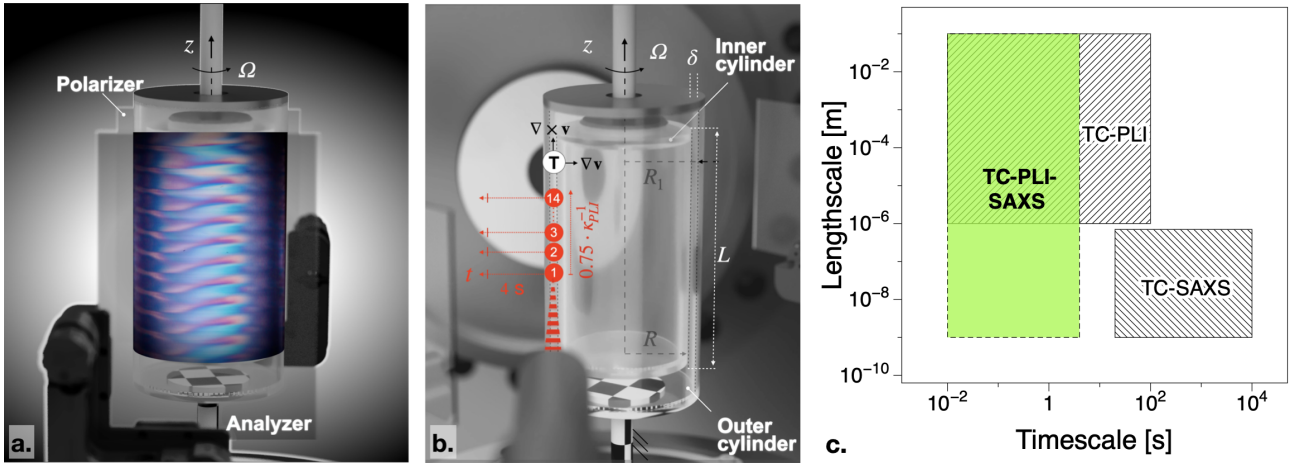


**Fig. 1** Custom Taylor-Couette experimental setup for multiscale analysis of nanoparticle suspensions in supercritical flows. **a**, Illustration of the PLI visualization setup consisting of transparent concentric cylinders and cross-polarizer setup illuminated from the background with LED lights (not shown) and as viewed from the optical visualization camera (not shown), exemplifying wavy vortex flow. **b**, Tangential configuration (denoted by a circled T) of the SAXS experiment on the same flow cell, during which a set of fourteen SAXS time series are collected as function of position along the vorticity direction. **c**, Accessible length and time scales of the present PLI-SAXS study (green), compared to previous state-of-the-art PLI [11] and SAXS [20] experiments in Taylor-Couette flow. The velocity gradient and vorticity directions are denoted by  $\nabla \mathbf{v}$  (or 2) and  $\nabla \times \mathbf{v}$  (or 3), respectively, where  $\mathbf{v}$  is the velocity vector (direction denoted by 1), positioned orthogonally to the planes formed by the afore mentioned axes.

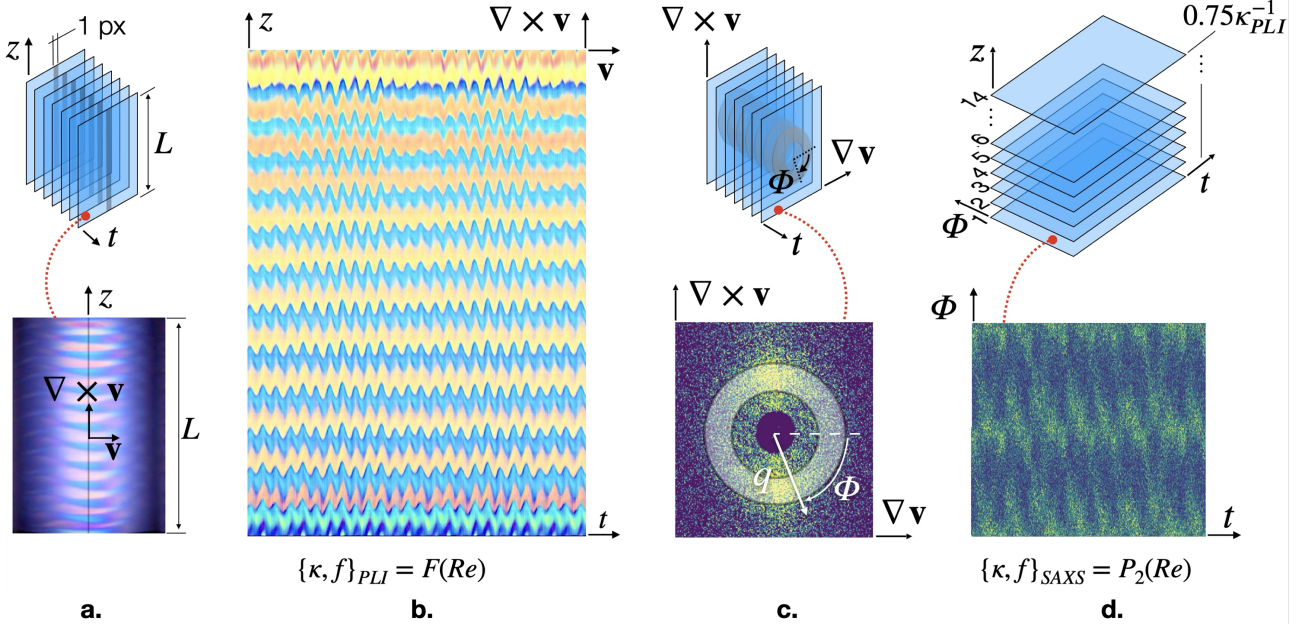


**Fig. 2** Summary of multiscale data analysis of TC-PLI-SAXS experiments. **a**, PLI video recordings processed as a sequence of frames wherefrom a line of 1 pixel is extracted along the vertical ( $z$ ) axis of the cylinders. **b**, Example of PLI space-time diagram constructed from the individual frames for modulated wavy vortices (MWV) in a CNC suspension. Following two-dimensional Fourier analysis, the macroscale characteristic wavenumber (spatial periodicity) and frequency(ies) (temporal periodicity),  $\{\kappa, f\}$ , of the MWV can be determined. **c**, SAXS data processing, starting from azimuthal integration of time series of scattering patterns over a range of scattering vector moduli  $q$ . **d**, From the azimuthally integrated data, the scattered intensity  $I(\Phi, z, t)_{q_0}$  can be determined for each  $z = ct$ . scan. Thereafter, for each time step the scattering anisotropy was determined using the Hermans orientation parameter  $P_2$ , with Fourier analysis thereof yielding nanoscopic, characteristic spatial and temporal frequencies.

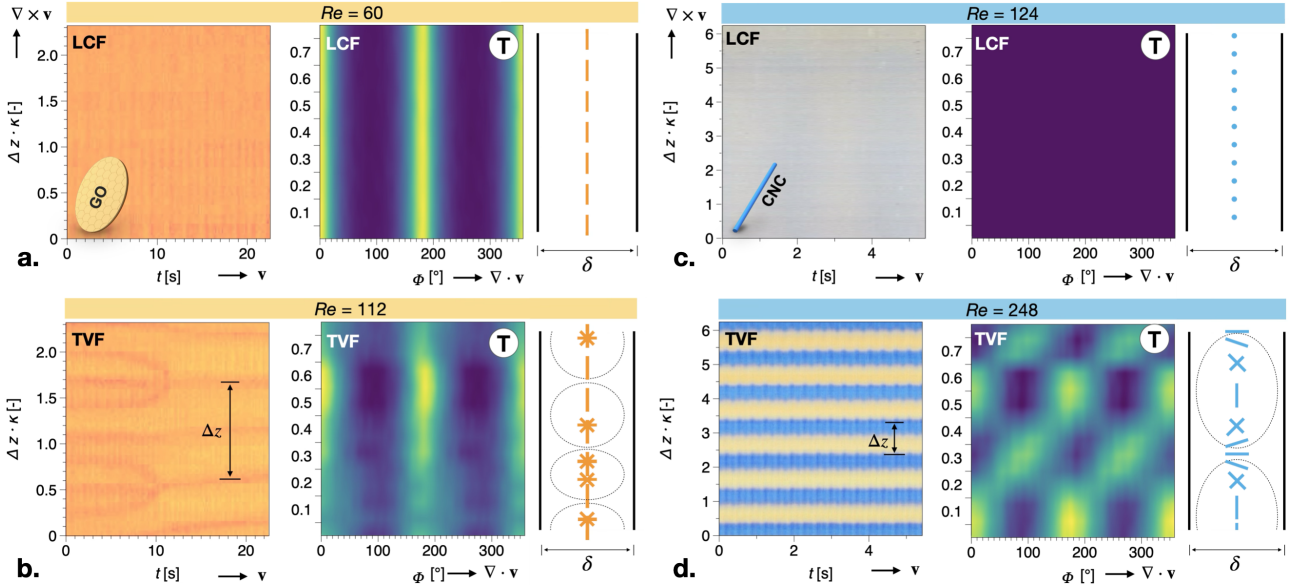


**Fig. 3** Multiscale observation of flow transitions. The data present the transition from **(a,c)** laminar Couette (LCF) to **(b,d)** Taylor vortex flow (TVF) for **(a,b)** the GO and **(c,d)** the CNC suspension. Each figure compares PLI visualization (left), temporally averaged azimuthally integrated SAXS data  $\langle I(\Phi, z)_{q_0} \rangle_t$  (middle), and a schematic picture of nanoparticle alignment based on the above data (right). Data collected in tangential configuration are highlighted with a circled T.

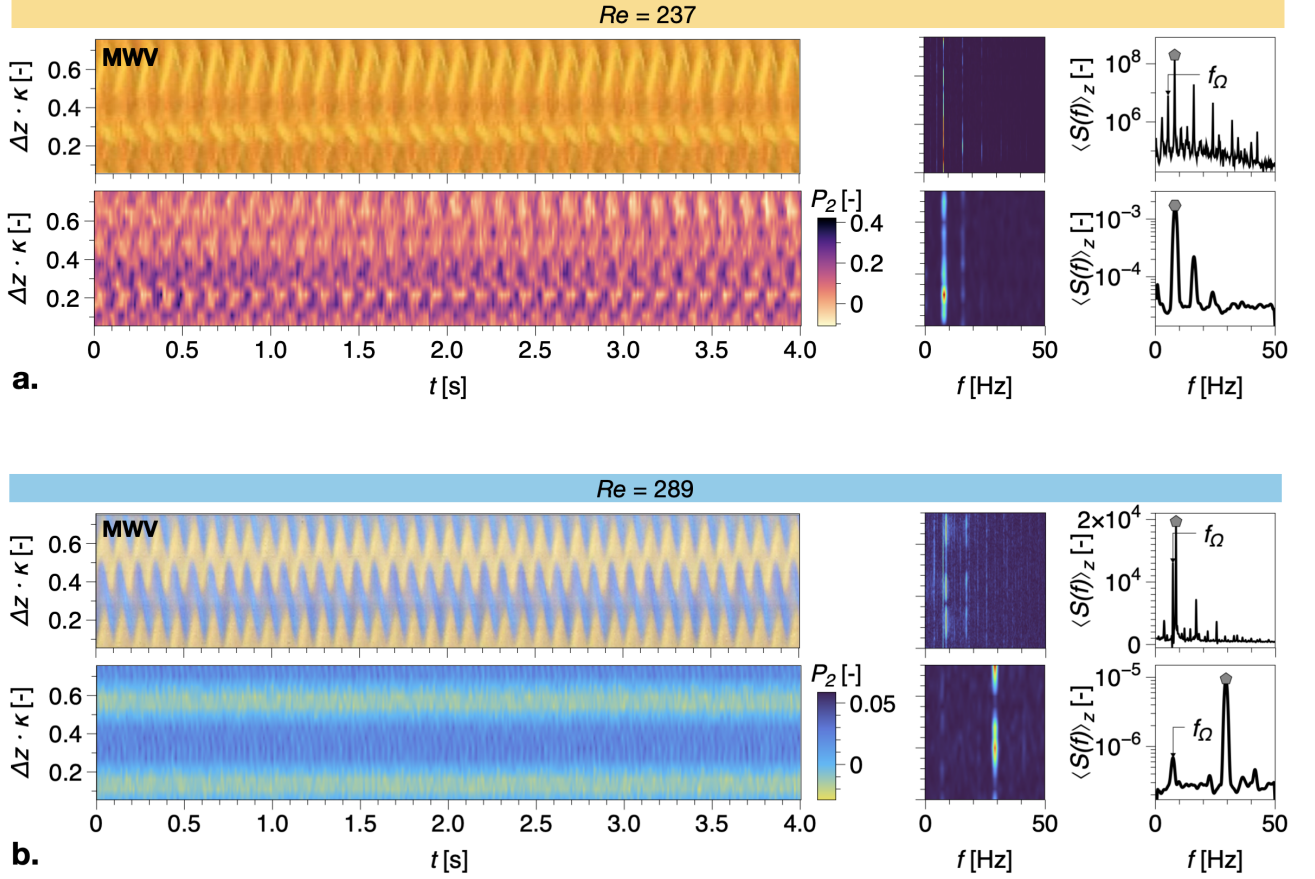


**Fig. 4** Multiscale spatiotemporal analysis of transitional flow in anisotropic nanoparticle suspensions. Data are presented for (a) GO and (b) CNC suspensions subjected to modulated wavy vortex flow (MWW). The left panel presents the macroscopic space-time plot obtained by PLI (top) and the spatiotemporally resolved nanoscopic Hermans orientation parameter  $P_2(z, t)$  determined by SAXS (bottom). The middle and right panels display spatially resolved  $S(z, f)$  and averaged  $\langle S(f) \rangle_z$  power spectral densities at both macroscopic (top) and nanoscopic lengthscales (bottom), determined by Fourier analysis from the data of the left panel. The rotational frequency  $f_\Omega$  of the Taylor-Couette cell and the characteristic frequency  $f_n$  (pentagon) are also depicted in the right panel. Note the common spatial scale for both PLI and SAXS.

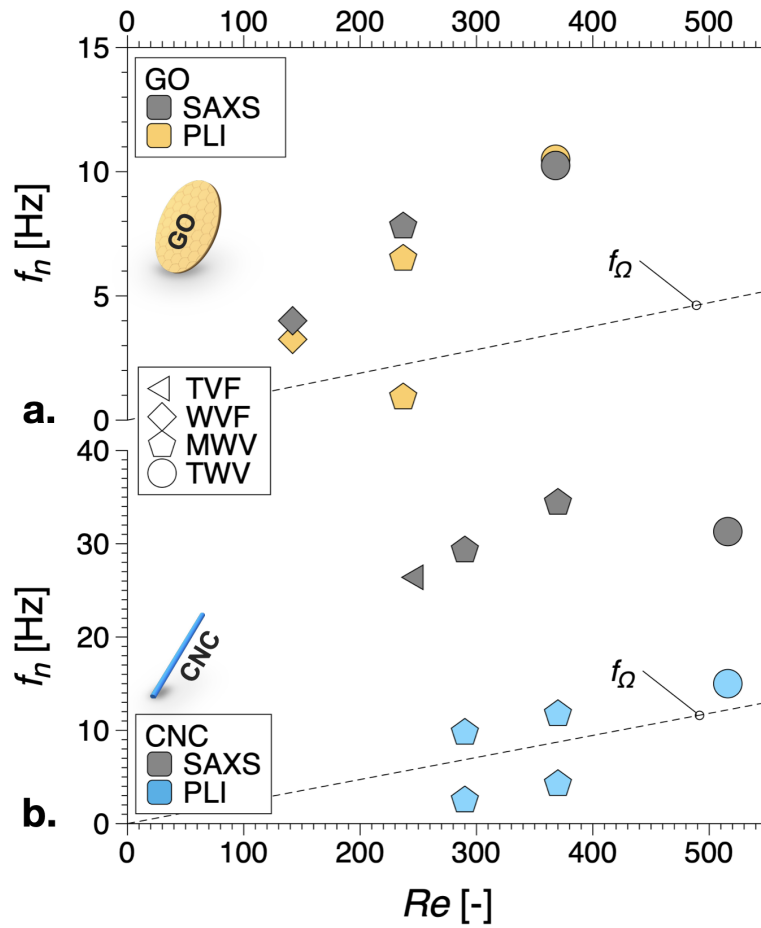
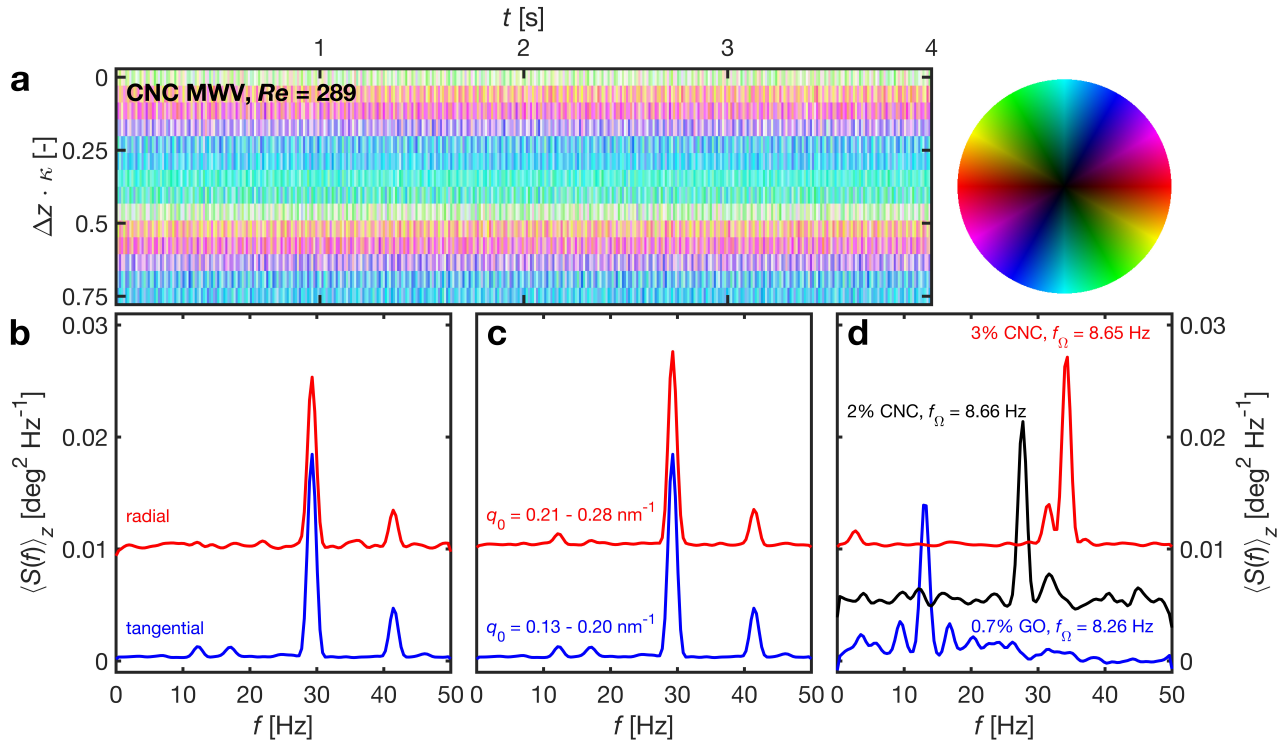
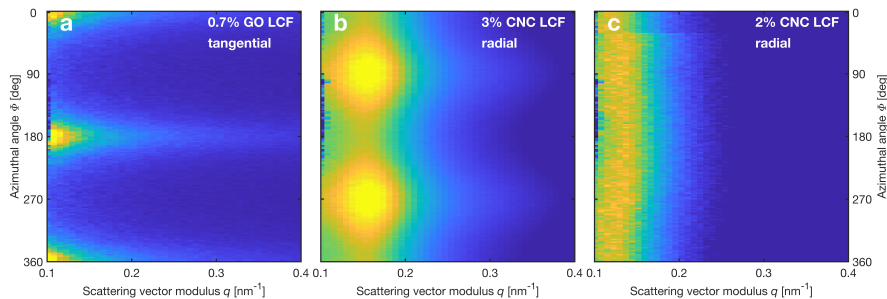


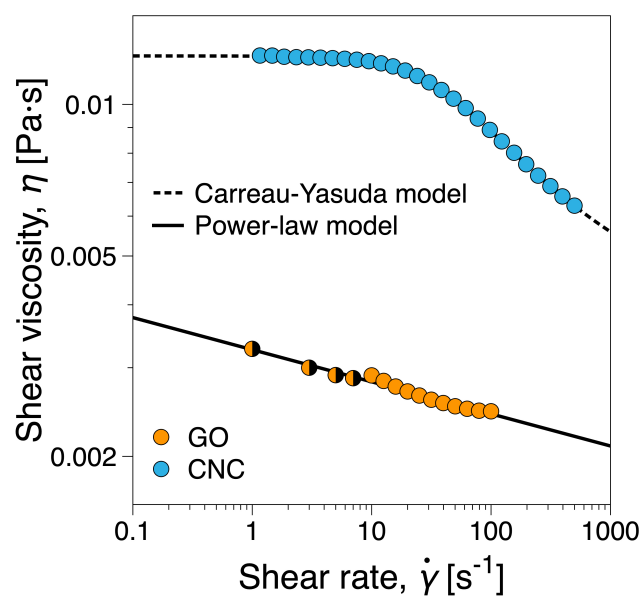
**Fig. 5** Multiscale dynamics of nanoparticle suspensions subjected to transitional flow. Both nanoscopic (SAXS) and macroscopic (PLI) data are presented for (a) GO and (b) CNC as the characteristic frequencies  $f_n$  versus Reynolds number  $Re$ . The dashed line depicts the rotational frequency  $f_\Omega$  of the Taylor-Couette cell. Note the different scale on the frequency axes for the GO and CNC data.



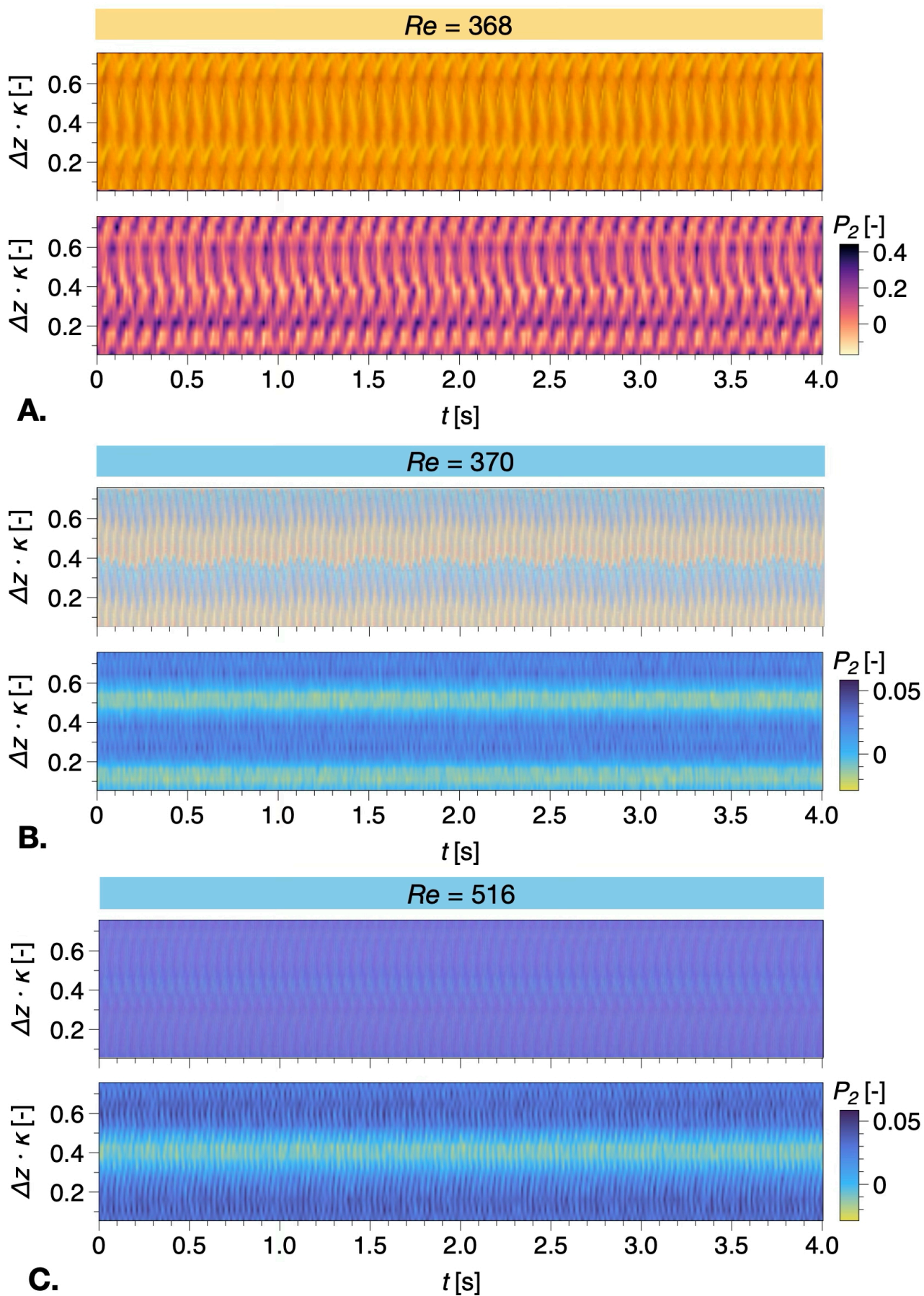
**Supplementary Fig. S6** Time-resolved scanning SAXS microscopy of nanoparticles under flow. **a**, Alternative FFT-based representation of the CNC MWV data in Fig. 4, with preferential alignment ( $\varphi$ ), degree thereof ( $|a_1|/|a_0|$ ), and scattering power ( $|a_0|$ ) encoded in the hue (cf. colour wheel), saturation, and value, respectively. The ensuing spatially averaged power spectral density  $\langle S(f) \rangle_z$  is presented for **(b)** different scattering configurations and **(c)** different scattering-vector range  $q_0$ , exhibiting no effect of scattering configuration or scattering-vector modulus. **d** Comparison of  $\langle S(f) \rangle_z$  for different suspensions - 0.7 wt% GO, 3 wt% CNC, and 2 wt% CNC - at comparable rotational frequency  $f_\Omega$  of the inner cylinder. The CNC suspensions show similar, fast nanoscale dynamics, whereas GO exhibits slower wavy dynamics, similar to what is expected based on the data of Fig. 5. The curves of panels **b-d** have been rescaled and vertically offset for clarity.



**Supplementary Fig. S7** Temporally averaged SAXS data acquired under laminar Couette flow (LCF). Data are collected from **(a)** GO in tangential and **(b)** CNC in radial scattering configuration, both shown as function of scattering vector modulus  $q$  and azimuthal angle  $\Phi$ . **c**, Data for a less concentrated CNC suspension are presented for comparison.



**Supplementary Fig. S8** Steady shear viscosity of the investigated suspensions. The half-filled symbols refers to long-term step input measurements, with each point starting for a fresh sample, in order to accurately reach steady-state. The 0.7 wt% GO and 3 wt% CNC data were fitted with the power-law and Carreau-Yasuda models, respectively.



Supplementary Fig. S9 Complementary data to the multiscale spatiotemporal analysis presented in Fig. 4. a, GO, b-c CNC.